# Development of Feature Tracking Code for analyzing Solar Spectropolarimetric Observation

**A Thesis**

submitted to
Indian Institute of Science Education and Research Pune
in partial fulfillment of the requirements for the
BS-MS Dual Degree Programme

by

Jharnesh Verma


Indian Institute of Science Education and Research Pune
Dr. Homi Bhabha Road,
Pashan, Pune 411008, INDIA.

May, 2025

Supervisor: Dr. Anusha L. S.

# Certificate

This is to certify that this dissertation entitled **Development of Feature Tracking Code for analyzing Solar Spectropolarimetric Observation** towards the partial fulfilment of the BS-MS dual degree programme at the Indian Institute of Science Education and Research, Pune represents study/work carried out by Jharnesh Verma at Indian Institute of Astrophysics, under the supervision of Dr. Anusha L. S., Assistant Professor, Theoretical Astrophysics, Indian Institute of Astrophysics during the academic year 2024-2025.

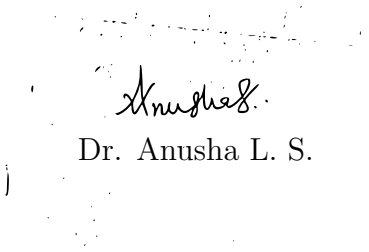

Dr. Anusha L. S.

Committee:

Dr. Anusha L. S.

Dr. Bhas Bapat

This thesis is dedicated to IIA

# Declaration

I hereby declare that the matter embodied in the report entitled **Development of Feature Tracking Code for analyzing Solar Spectropolarimetric Observation** , are the results of the work carried out by me at the Theoretical Astrophysics Indian Institute of Astrophysics under the supervision of Dr. Anusha L. S. and the same has not been submitted elsewhere for any other degree.

Jharnesh Verma
20201204
*5th year BS-MS student*

# Acknowledgments

I am grateful to my supervisor, Dr. Anusha L. S., for her continuous guidance and support throughout my thesis. Her professional and personal adivce was essential in carrying out this work, and she was always available to help me with any coding challenges I encountered. I would also like to thank Dr. Bhas Bapat, professor at IISER Pune, for his support. He is expert of my thesis project, and he had previously guided me through two semester projects at IISER Pune. Given that this work involved extensive coding, I acknowledge the various sources from which I learned programming. These include courses at IISER Pune—specifically an introductory Python course and a computational physics course—one of the projects under Dr. Bapat that required Geant4 simulations, and numerous YouTube tutorials.

I also wish to thank Dr. Sami K. Solanki and his group at the Max Planck Institute for Solar System Research (MPS), Göttingen, Germany, for providing the Solar Orbiter data. Additionally, I am grateful to Dr. Anusha and MPS for the opportunity to work on SUNRISE-1 data, one of the most advanced projects in the field of solar physics.

I would also like to thank my friends who supported me during this project, particularly those I met after joining IIA. Their assistance was instrumental throughout the project. In general, I extend my gratitude to the members of IIA, as my time there has provided me with a comprehensive understanding of astrophysics research. I had little knowledge of astrophysics research before, but now I can confidently say that I have gained significant insight into the research process.

Finally, I wish to thank my parents and grandparents for their continuous support. Their encouragement to attend IISER Pune and IIA has been fundamental in helping me pursue my dream of becoming a researcher. I am who I am today because of them.

# Abstract

Feature tracking is an important tool for studying the evolution of small-scale magnetic features on the Sun. It helps in analysing processes like bipolar magnetic emergence (BME), where loops of magnetic fields rise through the solar surface, and track events like splitting, merging, and cancellation of magnetic fields. The project aims to develop adaptable feature-tracking software for solar data obtained from high-resolution observations by the Sunrise balloon-borne solar observatory by converting IDL-based algorithms from Anusha et al. (2017) into C++. This transition will make the software more versatile, efficient, and suitable for analysing a broader range of solar datasets. The newly developed code will be applied to Solar Orbiter PHI data.

# Contents

# Part I

# Introduction

# Chapter 1

# Introduction

Solar magnetic fields drive many of the dynamic phenomena on the Sun. They are present in large structures like sunspots and active regions as well as in many small-scale magnetic elements found in the quiet Sun. In recent years, high-resolution spectropolarimetric data have greatly improved our understanding of these small features by observing their short-lived and changing behaviour. This thesis focuses on developing an optimized feature tracking code created in [1] to track these magnetic features in solar data.

## 1.1 Background and Significance

The quiet Sun, which covers regions without sunspots or large active areas, is known to contain a network of weak magnetic fields. Although each of these Internetwork (IN) fields is weak, together they contribute a large portion of the Sun's magnetic flux. Studying these fields is important for understanding basic processes like magneto-convection, local dynamo action, and how magnetic flux is recycled in the solar atmosphere [see 29, 28].

High-resolution instruments such as the Imaging Magnetograph eXperiment (IMaX) on the SUNRISE balloon and the Polarimetric and Helioseismic Imager (PHI) on the Solar Orbiter have provided detailed spectropolarimetric data [2, 31, 30]. These data include all four Stokes parameters, which allow us to determine the magnetic field vector using methods such as Zeeman polarimetry and the centre-of-gravity (COG) method [28]. However, because

of the complexity and dynamic evolution of these magnetic features, algorithms are needed to identify, track, and analyse them.

## 1.2 Context and Thesis Questions

The main questions we address in this work are:

1. How do we follow the evolution of small-scale magnetic features in high-resolution spectropolarimetric data?
2. How to optimize the already existing algorithm for efficiency?
3. How can such an algorithm be applied to other similar datasets?

These questions are important because understanding the behaviour and interactions of small-scale magnetic elements is key to building better models of solar magnetoconvection and the local dynamo [29, 28]. Better feature tracking can lead to more precise measurements of magnetic flux, which affects energy transport and heating in the solar atmosphere.

## 1.3 Scope of the Work

This thesis focuses on the theoretical and computational aspects of tracking features in solar spectropolarimetric observations. The scope includes:

- Improving the developed algorithm in [1] to automatically identify and track small-scale magnetic features over time in multi-dimensional datasets.
- Apply the newly developed code to SO/PHI dataset which has similar spatial and temporal resolution.

This work does not address data reduction or direct comparison with observational results. Instead, it emphasises on computational methods for tracking and analysing the evolution of solar magnetic features.

## 1.4 Goals of the Project

The primary goal of this project is to create a flexible and high-performance feature tracking code in C++ that extends earlier IDL-based methods [1]. This new code is intended to overcome the performance limits of previous methods and process large high-resolution datasets more effectively. The specific objectives are to:

1. Improve computational efficiency and scalability to manage complex, multi-dimensional datasets.

2. Apply the code to other datasets because the algorithm can be used to analyse broad range of data with similar spatial and temporal resolution.

# Part II

# Data

# Chapter 2

# Spectropolarimetric Observations

## 2.1 SUNRISE/IMaX

The high-resolution timeseries data analysed in this study were obtained during the first science flight of SUNRISE in June 2009 [2], providing novel spatial and temporal precision for quiet-Sun magnetic field observations. The dataset, captured by the Imaging Magnetograph eXperiment (IMaX) instrument, enabled detailed tracking of magnetic feature evolution with notable cadence and resolution. Observations were conducted on the Fe I 525.02 nm spectral line, utilizing advanced image reconstruction techniques to enhance clarity[11]. The following are the key details of the dataset:

- **High-Resolution Observations**: Data from 42 magnetograms with a spatial sampling of 40 km per pixel and 0.15–0.18″ angular resolution.
- **Cadence**: Time-series recorded every 33 seconds, allowing precise observations of features.
- **Spectral Sampling**: Measurements taken at ±40 mÅ and ±80 mÅ from the Fe I 525.02 nm line center, plus a continuum point 227 mÅ away.
- **Image Quality**: Phase-diversity reconstruction applied, removing 108 border pixels but significantly improving image clarity.

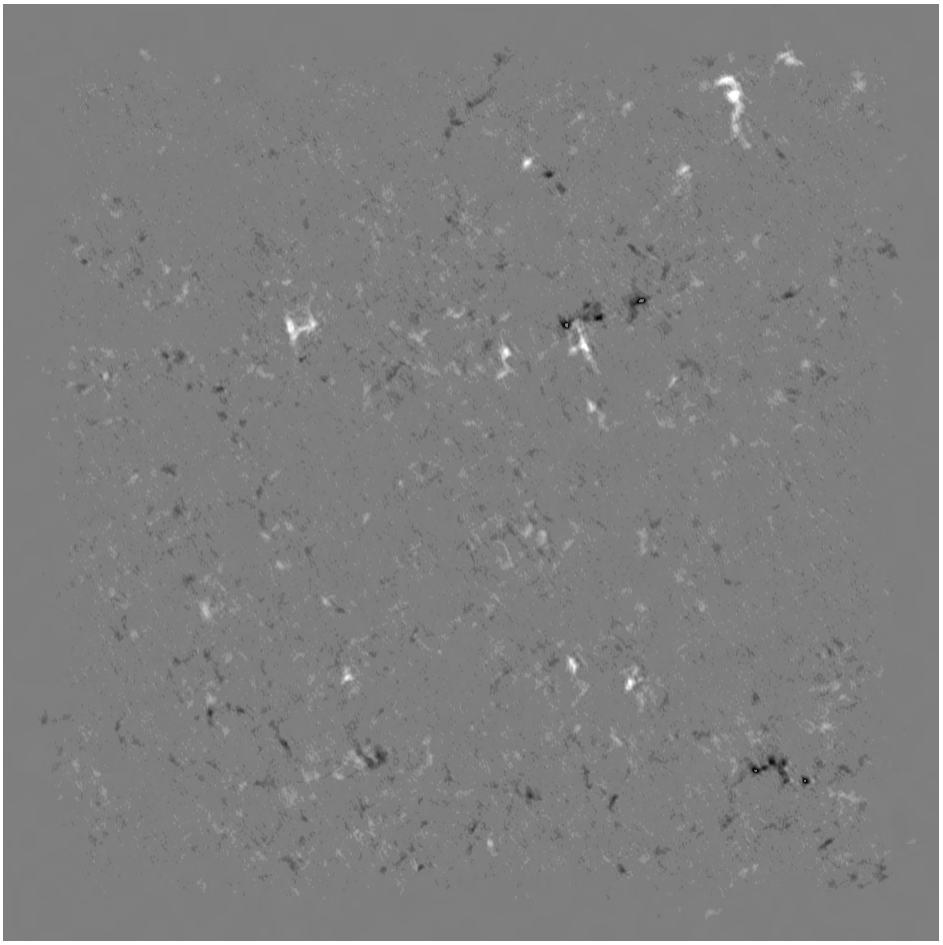

Figure 2.1: First time-frame of raw data of SUNRISE/IMaX data

- **Data Structuring**: Each time step forms a 5D data array with spatial and temporal coordinates $(x, y, t)$ for 4 Stokes Indices and 5 different wavelength points (including continuum).

- **Noise Level**: Reconstructed IMaX magnetograms have a noise level of $3 \times 10^{-3} I_c$.

- **Effective Field of View**: $43'' \times 43''$ coverage after processing.

- **Focus on Stokes $I$ & $V$**: The Stokes $I$ & $V$ measurements are used because of their correlation with the magnetic field.

- **Data Normalization**: Stokes $I$ & $V$ values normalized using spatially averaged continuum intensity $\bar{I}_c$.

- **Magnetic Field Computation**: Feature identification is based on Stokes averaged in wavelength $V/\bar{I}_c$, while the line-of-sight magnetic field is calculated separately from the individual Stokes $I$ & $V$ at each wavelength.

## 2.2 SO/PHI

The high-resolution timeseries dataset analysed in this study was obtained from the Solar Orbiter mission on April 10, 2023, using the Polarimetric and Helioseismic Imager (PHI) aboard the High-Resolution Telescope (HRT) [4]. This dataset offers unprecedented spatial and temporal precision for studying quiet-Sun magnetic features.

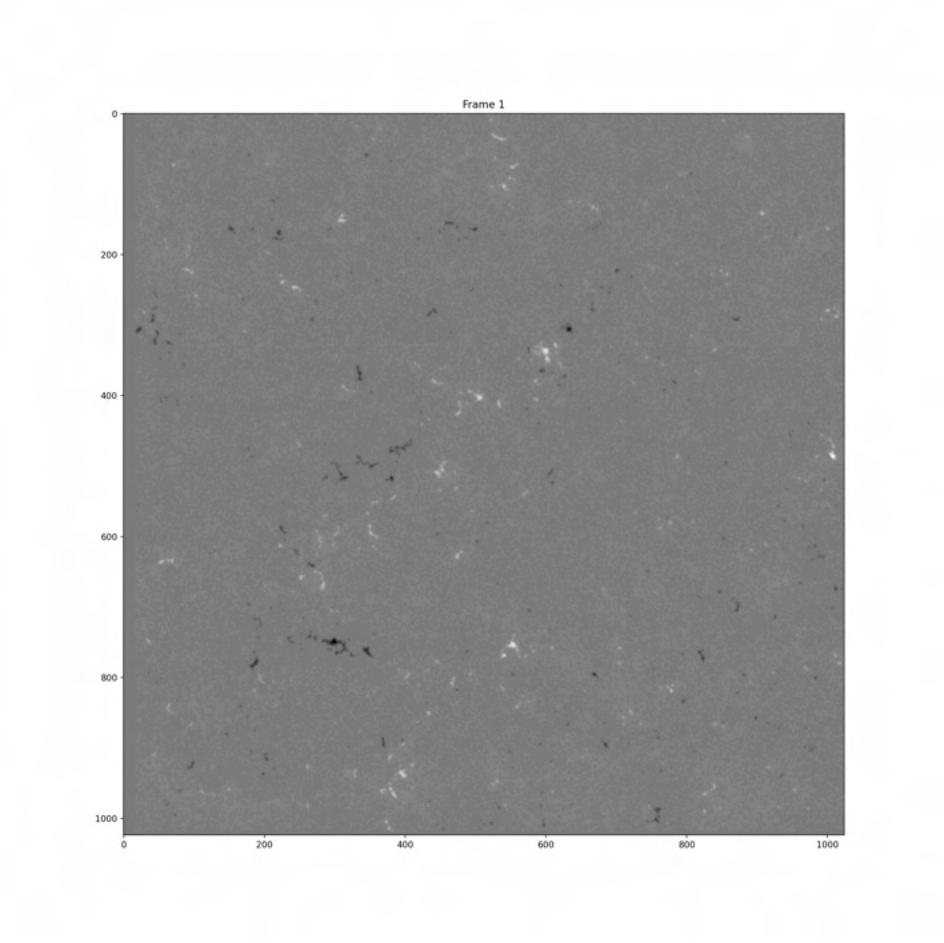


Figure 2.2: First time-frame of raw data of SO/PHI data

- **Dataset Characteristics:**
  - 360 magnetograms with a spatial resolution of $1024 \times 1024$ pixels.
  - Cadence of 60 seconds.
  - Captures six Stokes parameters.
  - Acquired in the $Fe\,I$ 6173 Å spectral line.
- **Spectral Sampling:**
  - Six discrete wavelength positions: 6173.184, 6173.253, 6173.323, 6173.391, 6173.461, and 6173.62 Å.
  - The final position serves as the continuum reference.
  - Characteristic wavelength: 6173.341 Å.
- **Data Processing and Quality:**
  - Phase diversity reconstruction applied (resulting in the loss of some border pixels).
  - Data normalized using the spatially averaged continuum intensity $\bar{I}_c$.
  - Noise level: $\sigma = 1.13 \times 10^{-3}$.
- **Data Structure and Format:**
  - Each time step is a 4D data array with temporal and spatial coordinates $(t, x, y)$ for 6 wavelength positions.
  - Pixel scale: 0.5 arcsec/pixel in helioprojective Cartesian coordinates.
  - First and last time steps excluded to minimize boundary effects.
  - Stored in FITS format with 8-bit pixel depth and lossless high-quality compression.
- **Stokes Parameters:**
  - Analysis focuses on Stokes $I$ and $V$.
  - The line-of-sight magnetic field is derived from individual Stokes $I$ and $V$ measurements, while $\bar{I}_c$ is used for normalization.

# Part III

# Theory

# Chapter 3

# The Dynamical Sun

The Sun, a G2V-type main-sequence star, is the dominant celestial body of our solar system. As an average-sized star among billions in the Milky Way, it serves as a fundamental reference for understanding stellar physics. With a mass of approximately $1.989 \times 10^{30}$ kg and a radius of about 696,340 km, the Sun contains 99.8% of the total mass of the solar system [21].

The Sun undergoes nuclear fusion at its core, converting hydrogen into helium and releasing large amounts of energy in the form of electromagnetic radiation. This process maintains a core temperature of nearly 15 million Kelvin, with energy gradually transported outward through radiation and convection[22] . The Sun's surface, or photosphere, emits radiation with an effective temperature of about 5,778 K[22]. Surrounding this layer are the chromosphere and corona, the latter of which extends millions of kilometres into space and is visible during solar eclipses.

Solar activity, driven by the Sun's magnetic field, manifests itself in phenomena such as sunspots, solar flares, and coronal mass ejections. The 11-year solar cycle modulates these activities, influencing space weather and impacting Earth's magnetosphere. Observations of the Sun through various missions, such as the Solar Orbiter, the Solar and Heliospheric Observatory (SOHO) and the Parker Solar Probe, have significantly enhanced our understanding of its complex behaviour.

## 3.1 Solar atmosphere

The Sun's atmosphere is a complex and dynamic region, which extends from the visible surface (the photosphere) to the outermost layer (the corona), which gradually merges into interplanetary space. The Sun's atmosphere is structured by its intense magnetic field, which produces phenomena such as sunspots, flares, and prominences. The transition between layers is marked by dramatic temperature variations, with the photosphere at approximately 5,778 K [8], rising through the chromosphere to reach more than a million Kelvin in the corona [22]. Understanding the atmosphere of the Sun is crucial for studying solar activity, space weather, and influence of the Sun on planetary environments.

### 3.1.1 Photosphere

The photosphere is the lowest layer of the solar atmosphere and the source of visible light. It has a depth of approximately 500 km and a temperature ranging from about 6,400 K at the bottom to 4,400 K at the top [22, 21]. The photosphere exhibits several key features:

- Granulation: A pattern of convection cells where hot plasma rises in bright granules, cools, and sinks at darker intergranular lanes. Each granule has a typical size of 1,000 km and a lifetime of about 5 – 10 minutes [23, 22].
- Sunspots: Magnetically active regions appear as dark patches. Sunspots are linked to strong magnetic fields that suppress convection, leading to lower temperatures (4,000 K)[22].
- Limb Darkening: Decrease in brightness toward the Sun's edge, caused by varying optical depth along the line of sight.

### 3.1.2 Chromosphere

Above the photosphere lies the chromosphere, a thin layer extending about 2,000 km in height. During total solar eclipses, the chromosphere appears as a reddish ring due to strong hydrogen-alpha (H$\alpha$) emissions at 656.3 nm. Key features include:

- Spicules and Mottles: Jet-like structures, that rise and fall and carry hot plasma upward at speeds of 25 km/s [24]. These structures are linked to magnetic field concentrations and supergranular flow patterns.

- Temperature Increase: The chromosphere exhibits an increase in temperature from 4,500 K at the bottom to 25,000 K at the top [25]. This heating is hypothesized to be driven by magnetohydrodynamic (MHD) waves and magnetic reconnection.

### 3.1.3 Corona

The corona is the Sun's outermost atmosphere and has temperatures exceeding 1–2 million K [8]. It extends millions of kilometers into space. Important aspects of the corona include the following:

- High Temperature and Ionization: Despite its high temperature, the corona has an extremely low density ($10^9$ particles per $cm^3$) [8]. Highly ionized atoms (e.g., Fe X–Fe XIV) emit intense forbidden spectral lines, revealing coronal magnetic structures.

- Magnetic Structure and Solar Wind: The corona is structured by magnetic fields that form loops, streamers, and coronal holes. Coronal holes are regions of open magnetic field lines that allow the high-speed solar wind to escape.

- Heating Mechanisms: The coronal heating problem remains an important question in solar physics. Possible explanations include wave heating (Alfvén waves dissipating energy) and magnetic reconnection (conversion of magnetic energy into heat and kinetic energy).

## 3.2 Photosphere

The photosphere is the visible surface of the Sun and the lowest layer of the solar atmosphere. The primary mechanism of energy transport in the photosphere is convection, which is seen as granulation [22]. The properties of the photosphere provide crucial information on the Sun's overall structure, dynamics, and energy output. Observations of the photosphere provide

direct evidence for solar magnetic activity, oscillations, and the processes of radiative energy transfer.

### 3.2.1 Convection

Convection plays a fundamental role in transporting energy from the interior of the Sun to its surface. The Sun's core generates energy through nuclear fusion, which releases energy as radiation. Due to the increased opacity of the plasma in the outer layers, convection becomes the dominant mode of energy transport in the outer 30% of the solar radius [3] [10]. The photosphere is where this convective energy transport ends, and energy is finally released into space.

#### Upflow and Downflow

Convection in the photosphere is characterized by a continuous exchange of hot and cold plasma. The upflowing plasma originates from the deeper convection zone and rises due to buoyancy, forming bright granules at the surface. These granules can reach speeds of several kilometers per second. As the plasma cools, it loses energy through radiation and becomes denser, sinking into the intergranular lanes as it downflows. The downflow regions are darker because of their lower temperatures and are often found at the edges of granules.

#### Granulation

Granulation is the observable manifestation of convection in the photosphere. It consists of a pattern of bright and dark regions formed by convective cells. Each granule typically has a size of about 1,000 km and a lifetime of approximately 5 to 10 minutes [23]. Granulation can be observed using high-resolution telescopes such as the Daniel K. Inouye Solar Telescope (DKIST), which provides detailed imaging of individual granules and their temporal evolution. The figure illustrates a high-resolution image of solar granulation taken by DKIST. The bright regions correspond to hot, rising plasma, whereas the darker lanes indicate cooler, descending plasma. These images reveal fine details of the turbulence, energy transport, and magnetic interactions within the photosphere.

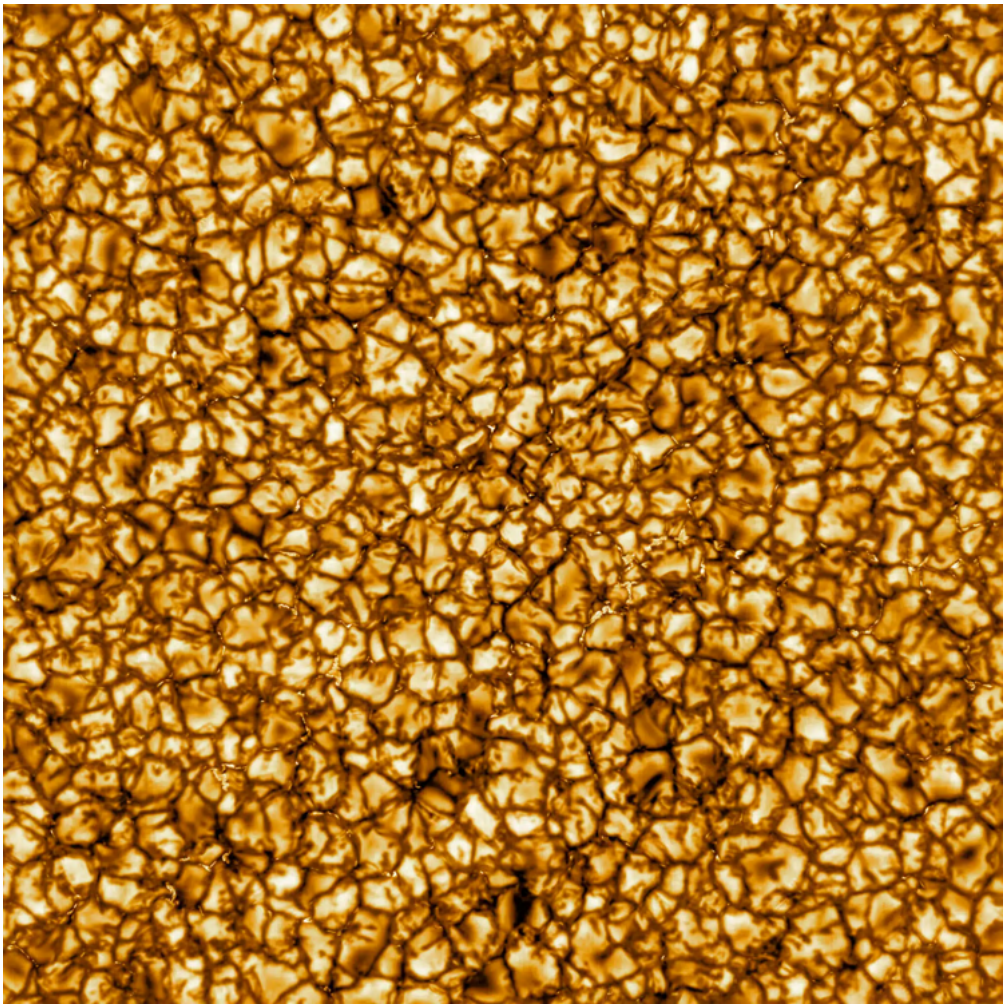

Figure 3.1: High-resolution image of solar granulation captured by DKIST. The bright granules represent rising hot plasma, while the darker intergranular lanes mark regions where cooler plasma is sinking. *Image credit: NSO/NSF/AURA*

## 3.3 Spectral Lines

Spectral lines provide a key understanding of the physical conditions of the Sun's atmosphere, including temperature, density, velocity fields, and magnetic fields. The formation of these lines occurs because of transitions between energy levels in atoms and ions, which absorb or emit photons at specific wavelengths. In the solar spectrum, absorption lines arise due to selective absorption by elements in the solar atmosphere, whereas emission lines appear in regions of higher excitation such as the chromosphere and corona. Two of the important spectral lines in solar physics are the neutral iron (Fe I) lines at 525 nm and 630 nm, which

are widely used to measure solar magnetic fields through the Zeeman effect [26].

### 3.3.1 Examples of Fe I Lines

#### Fe I 525 nm and 630 nm

The Fe I lines at 525.02 nm and 630.15 nm originate from neutral iron atoms and are widely used in spectropolarimetric studies of the Sun [11] [4]. They are sensitivity to the Zeeman effect, making them ideal for studying solar magnetism. These lines form at different heights in the photosphere, allowing the study of vertical variations in temperature and velocity fields[26].

- **Fe I 525.02 nm:** This line has a Landé factor of $g = 3.0$, making it highly sensitive to magnetic fields. However, it is also temperature dependent, which can complicate interpretations of magnetograms.
- **Fe I 630.15 nm and 630.25 nm:** These lines are slightly less magnetically sensitive than Fe I 525 nm but have been extensively used in solar magnetic field studies, including observations from the Hinode satellite and Solar-Orbiter.

### 3.3.2 Absorption Lines

#### Formation of Absorption Lines

Absorption lines in the solar spectrum result from the selective absorption of radiation at specific wavelengths by atoms in the outer layers of the Sun. The depth and shape of these lines depend on several factors:

- **Temperature:** Higher temperatures lead to increased excitation, affecting the line strength.
- **Pressure Broadening:** Collisional interactions can cause a broadening of the lines, leading to an increased line width.

- **Doppler Broadening:** Motion of absorbing atoms due to thermal motion or macroscopic flows shifts and broadens the line profile.

- **Magnetic Broadening:** The presence of magnetic fields can split absorption lines into multiple components due to the Zeeman effect[27].

### Non-LTE Effects in Absorption Lines

While many spectral lines in the photosphere can be analysed under the assumption of Local Thermodynamic Equilibrium (LTE), strong absorption lines often deviate from LTE conditions. This occurs because the source function $S_\nu$ differs from the Planck function $B_\nu$, leading to deviations in line intensities. Non-LTE effects are particularly significant in the chromosphere, where radiative transfer must be modelled using statistical equilibrium equations[26].

### Zeeman Splitting and Polarization

Magnetically sensitive absorption lines, such as Fe I 525 and 630 nm, exhibit Zeeman splitting when exposed to solar magnetic fields. This effect is used in spectropolarimetric observations to measure the strength and orientation of solar magnetic fields [5]. The degree of splitting is given by:

$$\Delta\lambda_B = 4.67 \times 10^{-5} g \lambda^2 B$$

where $g$ is the Landé factor, $\lambda$ is the central wavelength in nanometers, and $B$ is the magnetic field strength in Gauss. By analyzing the Stokes parameters (I, Q, U, and V), it is possible to infer the vector properties of solar magnetic fields[5].

## 3.4 Ground and Space-Based Instruments

The study of solar physics is dependent on observational facilities, both ground and space based. Ground-based telescopes provide high-resolution imaging and spectropolarimetry, while space-based instruments allow uninterrupted observations beyond the alterations due to the Earth's atmosphere. These observational platforms are essential for understanding solar magnetic fields, dynamics, and energy transport processes.

### 3.4.1 Ground-Based Instruments

Ground-based solar telescopes have significantly improved in resolution and instrumentation over the past several decades. Adaptive optics, high-resolution spectropolarimetry, and multiwavelength imaging have revolutionized our ability to probe solar fine structures and magnetic activity.

#### Swedish Solar Telescope (SST)

The Swedish 1-meter Solar Telescope (SST), located at the Roque de los Muchachos Observatory in La Palma, Canary Islands, Spain, is one of the most advanced ground-based solar telescopes[13]. It features an adaptive optics system that reduces atmospheric distortions, allowing for diffraction-limited observations in the visible and near-infrared spectrum.

Key capabilities of the SST include:

- High spatial resolution of approximately 0.1 arcseconds.
- Imaging spectropolarimetry using the CRISP and CHROMIS instruments.
- Investigation of sunspot fine structures, granulation, and magnetic elements.

#### GREGOR Telescope

GREGOR is a 1.5-meter solar telescope located at the Observatorio del Teide, Tenerife[14]. It is designed for high-resolution studies of solar magnetic fields. Unlike traditional vacuum

telescopes, GREGOR has an open-air design, which minimizes thermal turbulence inside the optical path.

Main features of GREGOR:

- Adaptive optics system for diffraction-limited imaging.
- Multi-wavelength spectropolarimetry in the visible and infrared.
- Large field-of-view capabilities for synoptic solar observations.

**Daniel K. Inouye Solar Telescope (DKIST)**

DKIST, with a 4-meter aperture, is the world's largest ground-based solar telescope. Located in Haleakal, Hawaii, DKIST is optimized for high-resolution imaging and spectropolarimetry[15]. It provides unprecedented details of solar magnetism and plasma dynamics by resolving features as small as 20 km on the solar surface.

Key aspects of DKIST:

- Advanced adaptive optics for near-diffraction-limited imaging.
- Full Stokes spectropolarimetry across a wide range of wavelengths.
- Studies of coronal heating, magnetic reconnection, and solar atmospheric dynamics.

### 3.4.2 Space-Based Instruments

Space-based solar missions are crucial for overcoming atmospheric limitations and allowing continuous observations of the Sun. These missions provide essential data on solar activity, magnetic fields, and atmospheric structures.

### SUNRISE

SUNRISE is a balloon-borne solar observatory that conducts high-resolution observations of the Sun's photosphere and chromosphere[2]. Notable contributions of SUNRISE:

- High-resolution imaging of the quiet Sun's magnetic fields.
- Observations of small-scale magnetic elements and convective processes.
- Polarimetric measurements that help understand magneto-convective interactions.

### Solar Orbiter

Solar Orbiter is a European Space Agency (ESA) mission launched to investigate the Sun's outer layers, its magnetic field, and the solar wind[32]. It follows an elliptical orbit that allows it to observe the Sun from high latitudes, providing a unique perspective on the solar poles.

- Studying the solar wind acceleration mechanism.
- Observing the Sun's polar magnetic fields and their role in the solar cycle.
- Investigating the connection between surface magnetic activity and heliospheric conditions.

### Parker Solar Probe

The Parker Solar Probe (PSP), launched by NASA in 2018, is the first spacecraft to enter the Sun's outer corona[16]. Using Venus gravity assists, PSP aimed to approach within 6.9 million km of the solar surface at speeds over 700,000 km/h. The purpose of Parker Solar Probe to investigate coronal heating, solar wind acceleration, and magnetic reconnection.

# Chapter 4

# Quiet Sun

The Sun's surface is dominated by magnetic activity, even in regions that appear devoid of sunspots and active regions. High-resolution spectropolarimetric observations have revealed that in such regions, collectively known as the **Quiet Sun**, there is a complex network of small-scale magnetic fields that play an important role in the global magnetic flux balance of the Sun. Understanding these fields is essential for understanding the Sun's influence on the heliosphere and its contribution to space weather phenomena.

Unlike active regions, where strong, concentrated fields shape large-scale structures such as sunspots and prominences, the quiet Sun magnetism is more dispersed and transient. It consists of two primary components:

- Network fields, which are concentrated along the boundaries of supergranular cells.
- Internetwork fields (IN), which emerge and evolve within these cells before dissipating or merging into the network.

Despite their relatively weak individual strengths, the total quiet Sun magnetic fields account for a significant portion of the Sun's total magnetic flux.

## 4.1 Characterization of Quiet Sun Magnetic fields

Solar magnetic fields are most effectively studied through polarized light, where stronger fields induce polarization in spectral lines via the **Zeeman effect**, while weaker fields influence scattering polarization through the **Hanle effect** [3]. Interpreting these polarization signals enables us to understand of magnetic field properties, which makes polarimetric observations a fundamental tool for investigating quiet Sun magnetism. The study of solar polarization involves measuring the four Stokes parameters $(I, Q, U, V)$, either fully or in selected combinations, across different spectral lines and wavelengths. These observations provide key information on the structure and dynamics of small-scale magnetic fields on the solar surface.

Understanding quiet Sun magnetism relies on three primary observational techniques:

1. Intensity-based magnetic proxies
2. Zeeman polarimetry
3. Hanle method

We will discuss Stokes parameters to understand Zeeman polarimetry in detail.

### 4.1.1 Stokes Parameters

The Stokes parameters $(I, Q, U, V)$ describe the state of polarization of electromagnetic radiation. These parameters are fundamental in astrophysical spectropolarimetry and are useful in characterizing the polarized light from the Sun, which is influenced by the Zeeman effect, scattering processes, and magneto-optical effects[19]. The Stokes vector is defined as:

$$\mathbf{S} = \begin{bmatrix} I \\ Q \\ U \\ V \end{bmatrix}$$

where:

- $I$ represents the total intensity of the radiation.
- $Q$ and $U$ describe the linear polarization.
- $V$ represents the circular polarization.

### Circular Polarization

Circular polarization occurs when the electric field vector of light rotates as the wave propagates. This is described by the Stokes parameter $V$, which is positive or negative depending on the polarization degree. In the presence of a magnetic field, circular polarization arises due to the Zeeman effect, where spectral lines split into right- and left-circularly polarized components.

For a weak magnetic field, the degree of circular polarization in a spectral line is given by:

$$\frac{V}{I} = 9.6 \times 10^{-4} B \cos\gamma$$

where $B$ is the magnetic field strength in Gauss and $\gamma$ is the inclination angle of the field relative to the observer's line of sight[20].

### Stokes $V$

The Stokes parameter $V$ quantifies circular polarization and is essential for measuring the longitudinal component of the magnetic field. The intensity profile of $V$ is antisymmetric with respect to the spectral line center, reflecting the Doppler shift of Zeeman-split components.

In the weak-field regime [3], $V$ is proportional to the derivative of the intensity profile:

$$V(\lambda) = -C B_{\text{LOS}} \frac{dI}{d\lambda}$$

where $C$ is a constant that depends on the *Lande'* factor of the spectral line. This

relationship is the basis for the magnetograph equation, used to infer line-of-sight (LOS) magnetic fields from spectropolarimetric observations.

#### LOS Magnetic Field

The line-of-sight (LOS) magnetic field component, $B_{\text{LOS}}$, is the projection of the total solar magnetic field along the observer's viewing direction. It is derived from the circular polarization signal using the relation:

$$B_{\text{LOS}} = \frac{1}{C}\frac{V}{I}$$

where $C$ is determined by the properties of the spectral line, including the Landé factor and height of formation [17]. This equation assumes the weak-field approximation, which is valid for most quiet Sun regions.

### 4.1.2 Zeeman Effect

The Zeeman effect describes the splitting of spectral lines in the presence of an external magnetic field, and is one of the most direct methods for measuring solar magnetic fields. The phenomenon was first observed by Pieter Zeeman and was later applied to astrophysical observations by George Ellery Hale, who detected magnetic fields in sunspots using this effect[5]. When a magnetic field is applied, atomic energy levels split into multiple Zeeman sublevels, where the number of sublevels equal angular momentum quantum number $J$. The transitions between these sublevels produce the Zeeman components of spectral lines. The wavelength shift $\Delta\lambda_B$ of these components is given by:

$$\Delta\lambda_B = 4.6686 \times 10^{-10}\lambda_0^2 g_{\text{eff}} B$$

where $\lambda_0$ is the initial wavelength, $g_{\text{eff}}$ is the effective Landé factor, and $B$ is the magnetic field strength [18].

Zeeman components are classified on the basis of their polarization properties:

- $\pi$-components ($\Delta M = 0$): Unshifted and linearly polarized perpendicular to the magnetic field.

- $\sigma$-components ($\Delta M = \pm 1$): Circularly polarized in opposite directions and shifted in wavelength according to field strength.

The ratio of Zeeman splitting to Doppler broadening, $\Delta\lambda_B/\Delta\lambda_D$, determines whether individual Zeeman components can be resolved [18]. When this ratio exceeds **1.5**, the splitting is sufficient to directly measure the magnetic field strength.

### 4.1.3 Zeeman Measurements

Different methods exist for detecting the Zeeman effect in solar observations, ranging from simple intensity measurements to full spectropolarimetric techniques.

**Stokes $I$ Measurements** Most spectral lines in the quiet Sun do not exhibit fully resolved Zeeman splitting due to weak fields. However, some infrared lines, such as Mg I 12.32 $\mu m$, display significant splitting even for moderate field strengths (hundreds of Gauss) [18]. This line is used to estimate the upper limits of the quiet Sun magnetic field strength.

For most photospheric lines, Zeeman broadening provides an alternative diagnostic tool. By comparing lines with different magnetic sensitivities, it has been estimated that quiet Sun magnetic fields were below 300 G in early studies and closer to 100 G in more recent analyses.

**Magnetograph Observations** Magnetographs measure the circular polarization ($V$) signal in Zeeman-sensitive lines to find the line of sight (LOS) magnetic field. The magnetic flux density $\Phi$ is estimated using[3]:

$$V(\lambda) = -f\Delta\lambda_B \cos\gamma \frac{dI}{d\lambda}$$

where $f$ is the magnetic filling factor, and $\gamma$ is the field inclination.

This technique is widely used in large-scale solar magnetic field measurements, such as those conducted by the Solar Dynamics Observatory (SDO) / Helioseismic and Magnetic Imager (HMI) and ground-based magnetographs.

**Full Stokes Spectropolarimetry** For a complete characterization of the vector magnetic field, full Stokes polarimetry is required. This involves measuring all four Stokes parameters $(I, Q, U, V)$, which describe intensity, linear polarization, and circular polarization.

The relationship between $Q, U$ and $V$ allows the determination of:

- LOS magnetic field ($B_{\parallel}$): Derived from Stokes $V$.
- Transverse magnetic field ($B_{\perp}$): Estimated from Stokes $Q$ and $U$.
- Azimuthal degeneracy: Fields with azimuths differing by $180^o$ produce identical $Q, U$ signals, leading to an inherent degeneracy.

Advanced spectropolarimeters, such as those on Hinode and DKIST, utilize inversion techniques to extract physical parameters from observed Stokes profiles.

**High Spatial Resolution**

The quiet Sun magnetic fields are not observable using conventional instruments. High spatial resolution is crucial to observe the cancellation of magnetic fluxes from oppositely polarized fields within a single resolution element. Advances in adaptive optics and space-based observations have largely improved spatial resolution. For example, SUNRISE data is a very high resolution data and has been employed in this thesis work. Enhanced resolution is essential for reducing uncertainties in the measured polarization signals.

## 4.2 The Quiet Sun Internetwork: Magnetic Properties and Theoretical Framework

The quiet Sun's Internetwork (IN) fields are weak, highly dynamic, and evolve on short timescales. Their study, combining high-resolution observations and magnetohydrodynamic (MHD) theory, is essential to understand solar magnetic flux distribution, energy transfer, and local dynamo action.

### 4.2.1 Magnetic Flux Distribution and Evolution

Compared to the network flux of $6.8 \times 10^{23}$ Mx, Internetwork fields contribute $\sim 1.1 \times 10^{23}$ Mx to the total solar flux, with individual features ranging from $10^{16}$ to $10^{18}$ Mx [3]. These fields emerge and disappear rapidly, with lifetimes of 10–20 minutes. The balance between flux emergence and removal is described by:

$$\frac{d\Phi}{dt} = S - L,$$

where $S$ represents flux emergence and $L$ accounts for removal via cancellation, disappearance, and movement towards network boundaries [3].

### 4.2.2 Zeeman effect and Field Strengths

Internetwork fields produce weak Zeeman signals, with Stokes $V$ amplitudes on the order of $10^{-3} I_{\rm QS}$. Line-of-sight field strength is inferred from:

$$V(\lambda) \approx -f \Delta\lambda_B \cos\gamma \frac{dI}{d\lambda},$$

where $\Delta\lambda_B = 4.6686 \times 10^{-10} \lambda_0^2 g_{\rm eff} B$. Observations indicate a broad range of strengths, typically 10–500 G, with kilogauss concentrations in some cases [18, 17, 3].

### 4.2.3 Local Dynamo and Magneto-Convection

Internetwork fields are sustained by a local turbulent dynamo, governed by the induction equation:

$$\frac{\partial \mathbf{B}}{\partial t} = \nabla \times (\mathbf{v} \times \mathbf{B}) - \nabla \times (\eta \nabla \times \mathbf{B}),$$

where $\mathbf{v}$ is the velocity field, and $\eta$ is the magnetic diffusivity [17]. Convective motions amplify weak seed fields, generating a continuous small-scale magnetic field with a power-law flux distribution.

### 4.2.4 Magnetic Interactions and Energy Transport

Internetwork fields evolve through splitting, merging, and cancellation. Opposite-polarity features undergo magnetic reconnection, contributing to heating. The flux loss rate is [18, 3]:

$$\frac{d\Phi_{\text{cancel}}}{dt} \approx -\alpha \Phi.$$

The high turnover rate of Internetwork flux suggests a crucial role in energy transport to the chromosphere and corona, which affects solar atmospheric heating and small-scale reconnection events.

### 4.2.5 Synthesis of Observational and Theoretical Perspectives

Observations from Sunrise/IMaX confirm that internetwork fields exhibit rapid flux emergence, advection, and cancellation, maintaining a quasi-steady flux balance. Theoretical models involving local dynamo processes and magneto-convective interactions reproduce the observed probability distribution functions of field strength and inclination, highlighting the self-sustaining nature of quiet Sun magnetism.

# Chapter 5

# Small scale magnetic features

A magnetic feature is theoretically defined as an adjacent set of spatial elements (pixels) for which the normalized circular polarization, $V/I_c$, exceeds a predetermined threshold. The area $A$ of a feature is given by the sum of the areas of the individual spatial elements that make up the feature. This definition allows for a consistent measure of the magnetic flux once the LOS field is computed via the COG method. A minimum area threshold is imposed to exclude features that are too small to be reliably resolved, ensuring that only statistically significant features are considered.

## 5.1 Flux Computation

In the theoretical analysis of quiet Sun Internetwork Magnetism, an essential step is the quantitative determination of the line-of-sight (LOS) magnetic flux within unresolved magnetic elements. A robust method for this purpose is the Center-of-Gravity (COG) technique, originally developed by [28], which computes the average LOS magnetic field from the displacement of the Stokes $V$ profile. In the framework of local thermodynamic equilibrium (LTE) line formation, the COG method is based on the principle that the centroid shift of the residual intensity profile in circular polarization provides a direct measure of the magnetic splitting and hence of the longitudinal field component.

For a spectral line with rest wavelength $\lambda_0$ and effective Landé factor $g$, the Zeeman

splitting is given by

$$\Delta\lambda_B = 4.6686 \times 10^{-10}\,\lambda_0^2\,g\,B, \tag{5.1}$$

where $B$ is the intrinsic magnetic field strength in Gauss and $\lambda_0$ is in angstroms. In the weak-field regime, the displacement of the centroid of the Stokes $V$ profile, $\Delta\lambda_G$, is defined as

$$\Delta\lambda_G = \frac{\int_{\lambda_1}^{\lambda_2} \lambda\, V(\lambda)\, d\lambda}{\int_{\lambda_1}^{\lambda_2} V(\lambda)\, d\lambda}, \tag{5.2}$$

where $V(\lambda)$ is the circular polarization, and the integration is performed over the wavelength interval $[\lambda_1, \lambda_2]$ encompassing the spectral line. The average LOS magnetic field, $B_{\rm LOS}$, is then obtained via

$$B_{\rm LOS} = \left| \frac{\Delta\lambda_G}{C_0\, g\, \lambda_0^2} \right|, \tag{5.3}$$

with the constant $C_0 = 4.67 \times 10^{-13}\,\mathrm{m^{-1}\,G^{-1}}$. The above equation is particularly advantageous as it is insensitive to Zeeman saturation effects, provided that the line weakening remains moderate.

In theoretical models, the above formulation is applied to each spatial element, and the resulting $B_{\rm LOS}$ is further spatially averaged over each identified magnetic feature to produce the field of average features, denoted as $\langle B_{\rm LOS}\rangle$. The magnetic flux $\Phi$ of a feature is then computed by

$$\Phi = A\,\langle B_{\rm LOS}\rangle, \tag{5.4}$$

where $A$ is the area of the feature. This approach, which does not involve an additional filling factor, assumes that the COG method intrinsically averages over unresolved fine structures within each resolution element.

It is important to note that the theoretical validity of the COG method [28], is based on the assumption that the spectral line is formed in an atmosphere with minor horizontal inhomogeneities. In a model in which the magnetic element is embedded in an undisturbed photosphere, the residual intensity profile is computed by subtracting the observed profile from the reference continuum intensity $I_c$. The centroid of this residual profile provides a measure of the magnetic splitting that is directly related to the LOS field. Under these conditions, the method yields an accuracy better than 10% for small line weakenings, making

it a preferred technique in theoretical studies of quiet Sun magnetism.

The above derivation is entirely independent of observational constraints; it is based solely on the theoretical principles of Zeeman splitting and radiative transfer in magnetized atmospheres. The COG method thus provides a model-independent measure of the average longitudinal magnetic field in unresolved flux elements, which is crucial for theoretical models of magneto-convection and local dynamo processes.

## 5.2 Definitions of Features, Parameters, and Events

A comprehensive theoretical framework for the evolution of small-scale magnetic features requires rigorous definitions of the features themselves as well as the various events and parameters that characterize their temporal evolution. This section presents the formal definitions and classification criteria used in theoretical analyses, abstracted from observational results.

### 5.2.1 Birth and Death of Magnetic Features

In the theoretical context, the evolution of a magnetic feature is delineated by its birth and death events. Specifically:

- **Birth by Appearance:** A feature is said to be born at time $t_2$ if the spatial location occupied by the feature at $t_2$ is devoid of any magnetic signal at the preceding time $t_1$. This definition captures the sudden emergence of magnetic flux into an otherwise quiet region.
- **Death by Disappearance:** Conversely, a feature is considered to have died at time $t_2$ if the magnetic signal previously present at time $t_1$ is absent at $t_2$. This disappearance can be attributed to processes such as flux cancellation or diffusion.

These definitions establish a temporal framework within which the lifetimes of individual features, denoted by $\tau$, can be computed as the interval between their birth and death.

### 5.2.2 Splitting and Merging Events

Magnetic features may undergo complex interactions during their evolution. Two primary types of interactions are considered:

- **Splitting:** A feature at time $t_1$ is said to split if it divides into two or more distinct features at time $t_2$. In this theoretical framework, if a parent feature splits, it is considered to have ceased to exist at $t_1$ (i.e., it "dies" by splitting), and the newly formed features at $t_2$ are treated as independent, newly born entities. A quantitative area-ratio criterion is employed to determine whether the splitting is significant; if the area of the largest child is substantially larger (e.g., by a factor of 2:1, 3:1, etc.) than that of the other child features, the largest child may be considered a continuation of the parent.

- **Merging:** When two or more features of the same polarity at time $t_1$ combine to form a single feature at time $t_2$, a merging event is said to occur. In this case, all the individual parent features are regarded as having ended at $t_1$, and the resulting merged feature is treated as a new feature at $t_2$. As with splitting, an area-ratio criterion is applied to decide if one parent dominates the merging process.

The classification of these events is critical in theoretical models because they directly affect the flux budget. The flux change associated with splitting or merging is determined by comparing the feature-averaged magnetic flux before and after the event.

### 5.2.3 Cancellation and Emergence

In addition to the unipolar events, interactions between features of opposite polarity are considered:

- **Cancellation:** This event occurs when magnetic features of opposite polarity come into contact and the net flux decreases. The flux loss rate during cancellation is described by

$$\frac{d\Phi_{\text{cancel}}}{dt} \approx -\alpha\Phi,$$

where $\alpha$ is an efficiency factor that encapsulates the rate of reconnection and flux annihilation.

- **Emergence:** Emergence events are characterized by the simultaneous appearance of spatially close features with opposite polarities. In a theoretical model, the total flux associated with an emergence event is given by the sum of the fluxes of the positive and negative features that appear concurrently or with a slight time offset.

Both cancellation and emergence are fundamental processes in the theoretical modeling of magnetic flux recycling in the quiet Sun, and they are incorporated into conservation equations governing the flux balance.

### 5.2.4 Mathematical Formulation of Flux Balance

The evolution of the total internetwork magnetic flux, $\Phi_{\mathrm{IN}}$, can be described by a conservation equation that accounts for all source and sink terms:

$$\frac{d\Phi_{\mathrm{IN}}}{dt} = \frac{d\Phi_{\mathrm{emerge}}}{dt} - \left( \frac{d\Phi_{\mathrm{cancel}}}{dt} + \frac{d\Phi_{\mathrm{disappear}}}{dt} + \frac{d\Phi_{\mathrm{transfer}}}{dt} \right).$$

In this formulation, $\frac{d\Phi_{\mathrm{emerge}}}{dt}$ represents the rate at which new flux is injected into the internetwork, while the loss terms represent flux removal via cancellation, disappearance, or advection to network regions. This equation is central to theoretical models of flux transport and underpins many numerical simulations of quiet Sun magneto-convection.

# Part IV

# Methods and Results

# Chapter 6

# Methods

In this thesis project, a feature tracking code in C++ was developed based on an earlier version of the same code written in IDL. The code development in general has three stages.

- Development
- Testing
- Validation/Verification

First we shall discuss the original/reference code which is in the IDL language. Subsequently, the programming languages used/tested for development will be discussed. Finally, how optimization was carried out will be discussed.

## 6.1 Reference Code

The reference code provides a comprehensive framework for identifying, tracking, and analysing small-scale magnetic features from solar spectropolarimetric observations. Stokes $V$ profile observations are used in the algorithm. Below is an interactive, point-wise breakdown of the algorithm.

### 6.1.1 Identification

**Overview:**

- Construct a 3D data cube by averaging the values over four wavelength channels.
- Apply a threshold (typically at $2\sigma$) to filter out noise and isolate significant features.
- Use binary masking to classify features by polarity (positive and negative).
- Number the features.

**Steps:**

1. **3D Array Creation:**
   - Compute the average with signs over four wavelengths.
   - During averaging, the +sign for wavelengths above the line centre and vice versa.
   - Store the result in a 3D array (e.g. dimensions $936 \times 936 \times 42$).
2. **Thresholding:**
   - Filter out values below the $2\sigma$ threshold, where $\sigma$ is the noise level.
   - Save the filtered data in a double precision array.
3. **Feature Detection (Lanefind):**
   - Generate binary masks for both positive and negative features.
   - Calculate the area of each detected structure.
   - Exclude features smaller than 8 pixels.
4. **Feature Numbering:**
   - Number all the 3D features starting from one to the maximum number.
   - 3D features are all the features connected across the 3D array.
5. **Data Storage:**
   - Combine the positive and negative masks into a comprehensive binary mask.
   - Store the processed data in an HDF5 file for further analysis.

**Removal of Boundary**

**Objective:**
- Eliminate features that touch the spatial boundaries at any time step because they cannot be tracked.

**Method:**
- Analyse the spatial coordinates of each feature.
- Discard any features intersecting the image edges.
- Generate visualizations (images/animations) to verify successful boundary removal.

**Substructures**

**Overview:**
- Further, differentiate 3D features into 2D substructures to capture finer spatial details.

**Process:**
- Identify connected regions within the binary mask.
- Label and index these substructures.
- Remove substructures with fewer than 4 pixels.
- Save the processed substructure arrays for additional analysis.

### 6.1.2 Dilation

**Purpose:**
- Enhance connectivity among detected features and facilitate temporal tracking.

**Operations:**
- Apply dilation to extend the boundaries of identified features.
- Compare neighbouring pixels across temporal slices to merge overlapping features.
- Estimate feature lifetimes and spatial extents by tracking dilated regions.

### 6.1.3 Flux Computation

**Method:**
- Utilize the Center-of-Gravity (COG) technique to compute the line-of-sight magnetic field.

**Steps:**

- Integrate the Stokes $V$ profiles normalized by the continuum intensity.
- Calculate the weighted wavelength shift $\Delta\lambda_G$ as:

$$\Delta\lambda_G = \frac{\int_{-\infty}^{\infty} V\,\Delta\lambda\,d\Delta\lambda}{\int_{-\infty}^{\infty}(I_c - I)\,d\Delta\lambda}.$$

- Compute the line-of-sight magnetic field:

$$B_{\mathrm{LOS}} = \left|\frac{\Delta\lambda_G}{C_0\,g\,\lambda_0^2}\right|,$$

  where $C_0 = 4.67 \times 10^{-13}\,\mathrm{m^{-1}G^{-1}}$, $g$ is the Landé factor, and $\lambda_0$ is the central wavelength.
- Average $B_{\mathrm{LOS}}$ over each feature to obtain a feature-averaged magnetic flux.

**Emergence Cancellation**

**Goal:**

- Quantify the processes of magnetic flux emergence and cancellation.

**Procedure:**

- **Tracking:** Compare consecutive time frames to determine feature evolution.
- **Emergence:** Measure the increase in flux from the birth of a feature to its maximum value.
- **Cancellation:** Identify overlaps between features of opposite polarities that lead to a reduction in net flux.
- **Flux Emergence Rate (FER):** Aggregate flux differences across the dataset to compute the FER.

## 6.2 Programming languages used for CODE optimization

### 6.2.1 IDL

- **Purpose:**

  - Initial platform used for the implementation of the feature-tracking algorithm (reference code).
  - Designed to hold high-level array operations and built-in visualization tools.

- **Features:**
  - Commonly used in astrophysics. Several algorithms have been previously developed in IDL, although other programming languages are also being used.
  - Simplified alteration of multidimensional datasets.
  - Built-in support for image processing.
  - Several inbuilt functions are quite useful. A characteristic exclusive to higher-level languages.

- **Limitations:**
  - Performance bottlenecks when processing large datasets.
  - Requires a paid license, limiting accessibility.
  - Memory management is less efficient compared to lower-level languages.

### 6.2.2 C++

- **Purpose:**
  - To overcome the performance and licensing issues encountered with IDL.
  - To provide more control over memory and computational efficiency.

- **Key Features:**
  - **Efficient Data Handling:**
    * Use of pointers, arrays, and `std::vector` for optimized memory management.
    * Conversion of 3D arrays into 1D vectors to facilitate HDF5 file storage.
  - **Parallel Processing:**

    - Implementation of OpenMP to parallelize computationally intensive loops.
    - Significant reduction in processing time (from approximately 1 hour to under 5 minutes).
  - **Optimized Algorithms:**
    - Restructured loops and removal functions to reduce iteration counts. Finally, reduced computation time to 30 seconds (from 1 hour) for the structure finding algorithm (lanefind).
    - Custom data structures to streamline feature identification and flux calculation.

- **Challenges Addressed:**
  - Synchronization issues during parallel processing.
  - Handling the storage limitations of HDF5 for multidimensional data.
  - Reorganizing bottlenecks, especially in a function that removes small features.

### 6.2.3 Python

- **Purpose:**
  - To complement the C++ core by handling post-processing tasks.
  - To facilitate the generation of visual outputs such as images and GIFs.
- **Key Features:**
  - **Visualization:**
    - High-level libraries (e.g., Matplotlib) are used for creating detailed images and animations.
  - **Ease of Scripting:**
    - Rapid development of scripts for data verification and result presentation.
  - **Integration:**

    - Acts as a bridge between the high-performance C++ code and user-friendly analysis tools.

### 6.2.4 Choosing C++

- **Performance Improvements:**
  - Drastically reduces processing time through low-level optimizations and parallel computing.
- **Resource Efficiency:**
  - Offers precise control over memory allocation and system resources.
- **Cost-Effectiveness:**
  - Eliminates the need for expensive licenses associated with proprietary software (e.g., IDL).
- **Scalability and Flexibility:**
  - Easily integrates with advanced libraries (such as HDF5) for efficient data storage.
  - Adaptable to evolving research requirements and capable of handling larger datasets.
- **In Scientific Research:**
  - Widely recognized for its usefulness and efficiency in scientific computing.

## 6.3 Optimization

### 6.3.1 C++ advantages

- **Improved Performance:**

  - Low-level optimizations and parallel processing (via OpenMP) significantly reduce runtime.
  - Optimized loops and reduced iteration counts allow processing to happen in minutes instead of hours.

- **Resource Efficiency:**
  - Direct memory management allows for control over large datasets.
  - Efficient use of data structures minimizes overhead.

- **Cost-Effectiveness:**
  - Transitioning from IDL to open-source C++ eliminates licensing costs.

- **Scalability:**
  - The modular design and optimized data handling are well suited for processing increasingly large observational datasets.

### 6.3.2 Challenges faced

- **Performance Bottlenecks:**
  - Early iterations and loops in feature removal functions were computationally heavy.

- **Parallel Processing Difficulties:**
  - Synchronizing access to shared data structures (e.g., 3D `std::vector`) posed significant challenges.

- **HDF5 Integration:**
  - Direct storage of multidimensional data required the conversion of 3D arrays to 1D, adding complexity.

- **Debugging Complex Code:**
  - Resolving memory corruption and ensuring thread safety in parallel code necessitated extensive debugging.

- "Segmentation fault" was a recurring problem which arises when a program attempts to access memory it is not authorized to access.

- **Multidimensional Pointer Arrays:**
  - Memory management of pointer arrays was difficult within loops and caused several "double-free or corruption" errors.

### 6.3.3 Restructuring changes

- **Loop Optimizations:**
  - Reorganized loops to avoid redundant computations.
  - Reduced the number of iterations in key functions (e.g., from $40 \times 936 \times 936 \times 21319$ iterations to a single pass per pixel).

- **Modular Code Design:**
  - Segmented code into different modules for feature identification, flux computation, and data storage.
  - This improved readability and maintainability.

- **Enhanced Parallelization:**
  - Introduced OpenMP to split heavy computations across multiple threads, reducing total runtime significantly.

### 6.3.4 Pointers and Vectors

- **Dynamic Memory Management:**
  - Utilized `std::vector` for dynamic array management, facilitating flexible data handling.

- **Direct Memory Access:**
  - Employed pointers for efficient and rapid memory access, crucial for processing large datasets.

- **Data Conversion:**
  - Converted 3D vectors into 1D vectors to ensure compatibility with HDF5 file storage.

### 6.3.5 HDF5

- **Efficient Data Storage:**
  - The HDF5 format is used to manage complex, multidimensional datasets efficiently.
  - Provides fast read/write capabilities essential for large solar data.
- **Implementation Challenges:**
  - Direct storage of 3D data is unsupported; hence, a conversion to 1D vectors is necessary.
  - Careful management of hierarchical data structures and metadata is required.

### 6.3.6 Large datasets

- **Handling High-Resolution Data:**
  - Designed to process 5D arrays (spatial, wavelength, and temporal dimensions).
  - Capable of handling data with 42 time steps and spatial dimensions of $936 \times 936$.
- **Scalability:**
  - Modular design and parallel processing facilitate scaling to even larger datasets.

### 6.3.7 Debugging

- **Issue Identification:**
  - Extensive debugging was performed to resolve issues in parallel code and pointer management.
  - Memory corruption and synchronization problems were identified through iterative testing.
- **Strategies and Tools:**
  - Profiling tools were used to pinpoint performance bottlenecks.
  - Python scripts were used to visualize intermediate outputs, helping verify the correctness.
  - Incremental testing and modular debugging strategies helped isolate errors effectively.
  - The printing values and arrays and the verification with IDL output was quite helpful and important.

## 6.4 Application of the code

To validate the newly developed code we apply the code to Sunrise data and compare the results obtained using original IDL and the new C++ codes.

# Chapter 7

# Results

## 7.1 SUNRISE

In this section we summarize the results that are already published in Anusha et al. (2017). The results presented here are generated from the newly developed C++ code and they are verified to match with the original results. For different modules, code output was printed in text files and verified. The output from IDL and newly developed C++ code matches perfectly for each module.

- Total number of features:
  - 3D (positive and negative):
    - Positive: 3853
    - Negative: 4106
  - 2D (positive and negative):
    - Positive: 25076
    - Negative: 25178

The 3D features, as mentioned before, are the group of pixels connected across both spatial and temporal dimensions. So, a 3D feature is formed by all the pixels connected in $x, y, t$.

| Module | Time taken by IDL | Time Taken by C++ |
|---|---|---|
| Lanefind3d | 30 mins | 30 secs |
| Lanefind2d | 20 mins | 5 mins |
| Dilation | 20 mins | 3 mins |

Table 7.1: Time Comparision

Similarly, 2D features are the ones only connected across $x, y$, i.e. only the spatial part. Since the minimum number of pixel size allowed is 8, there are significantly less 2D features than 3D.

### 7.1.1 Evolution of magnetic features

The first evolution image represents the raw normalized data with thresholds applied. The total number of time frames is 42. Here we see evolution every 5th frame.

The second evolution image is binary-masked, where white represents positive and black represents negative features. All positive features are given +1 and all negative ones are given -1. There are 40 total time frames. The evolution is clearly visible in this set of images. Black and white patches represent opposite-polarity features that emerged from the Sun's surface. The aim is to calculate the magnetic fluxes in:

1. Bipolar emergence
2. Cancellations

The third image is obtained by dilating the structures and binary masking them. These dilated features are used to identify if the two nearby features are the same or different. The evolution of dilated structures can be seen in the image.

### 7.1.2 Comparing the optimized code and original code

Below is the time comparison between the IDL and the C++ code for the SUNRISE data. Significant time reduction has been achieved, as can be seen below.

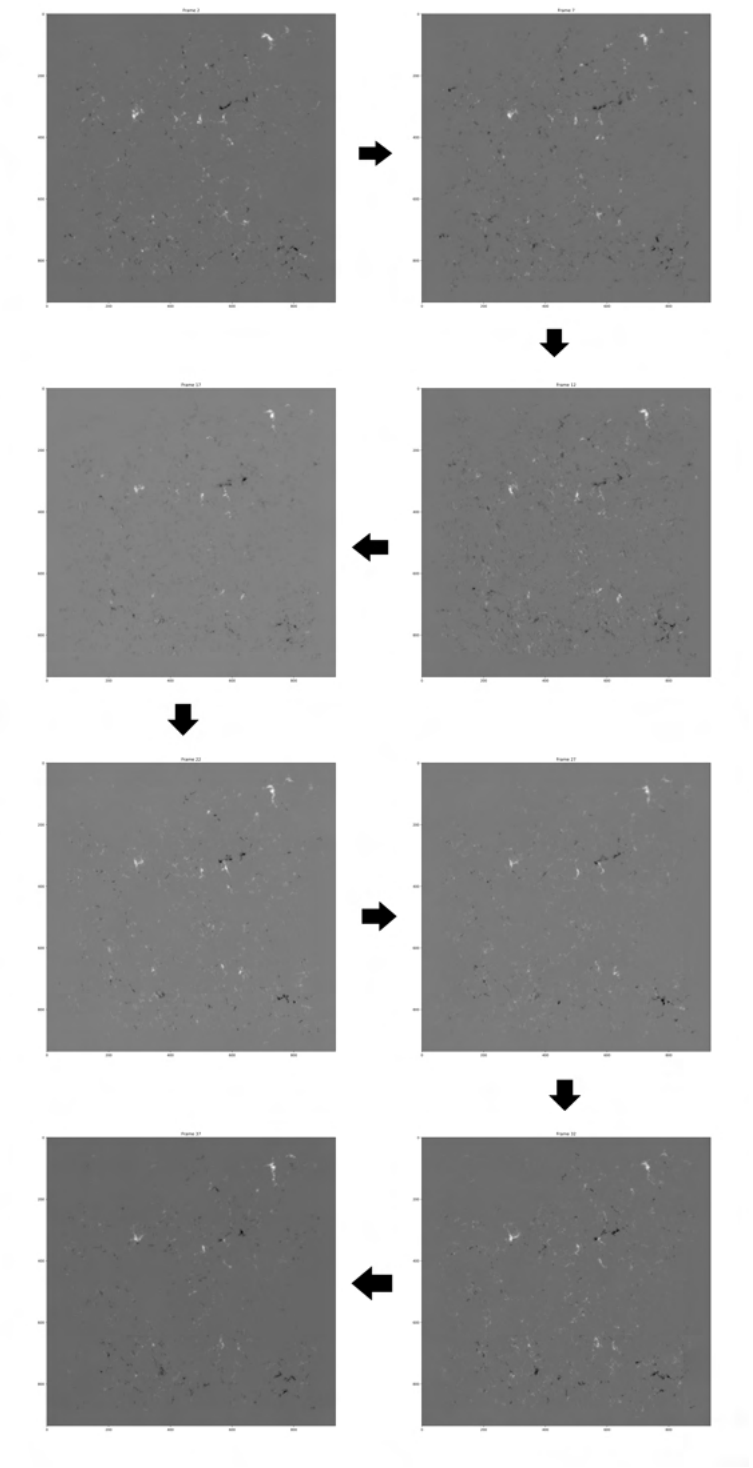

Figure 7.1: Raw data evolution for SUNRISE data

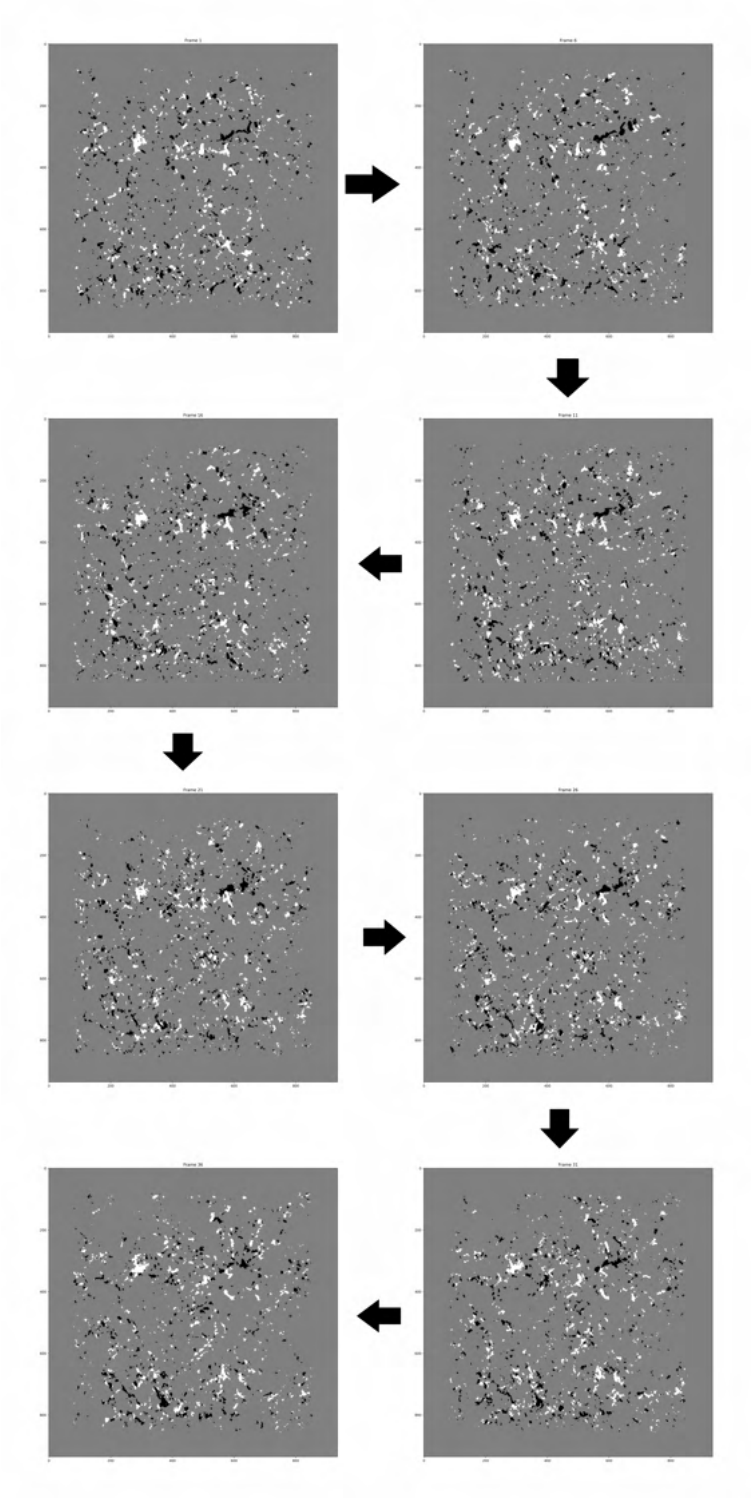

Figure 7.2: Binary masked features and their evolution for SUNRISE data

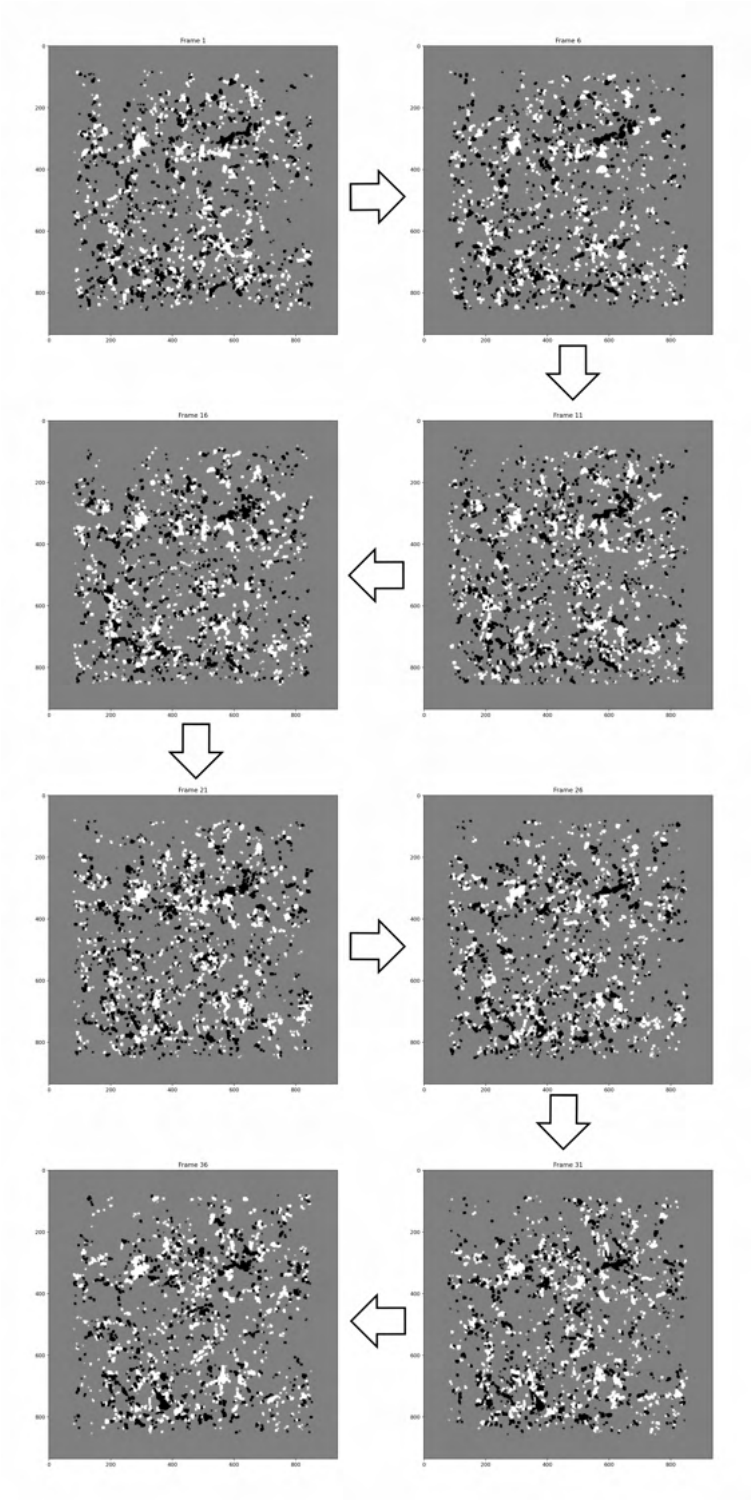


Figure 7.3: Dilated features and their evolution for SUNRISE data

## 7.2 SO/PHI

The newly developed C++ code was applied to SO/PHI data. The results obtained are presented below.

- Total number of features :
  - 3D (positive and negative):
    - Positive: 49172
    - Negative: 71573

### 7.2.1 Evolution of magnetic features

The first evolution image represents the raw normalized data with thresholds applied. The total number of time frames is 360. Here we see evolution every fifth frame.

## 7.3 Future work

The work presented here will be published in an international journal. The emergence-cancellation module is the only module left to be developed and optimized. Prior to that, the SO/PHI data is being applied to the developed code.

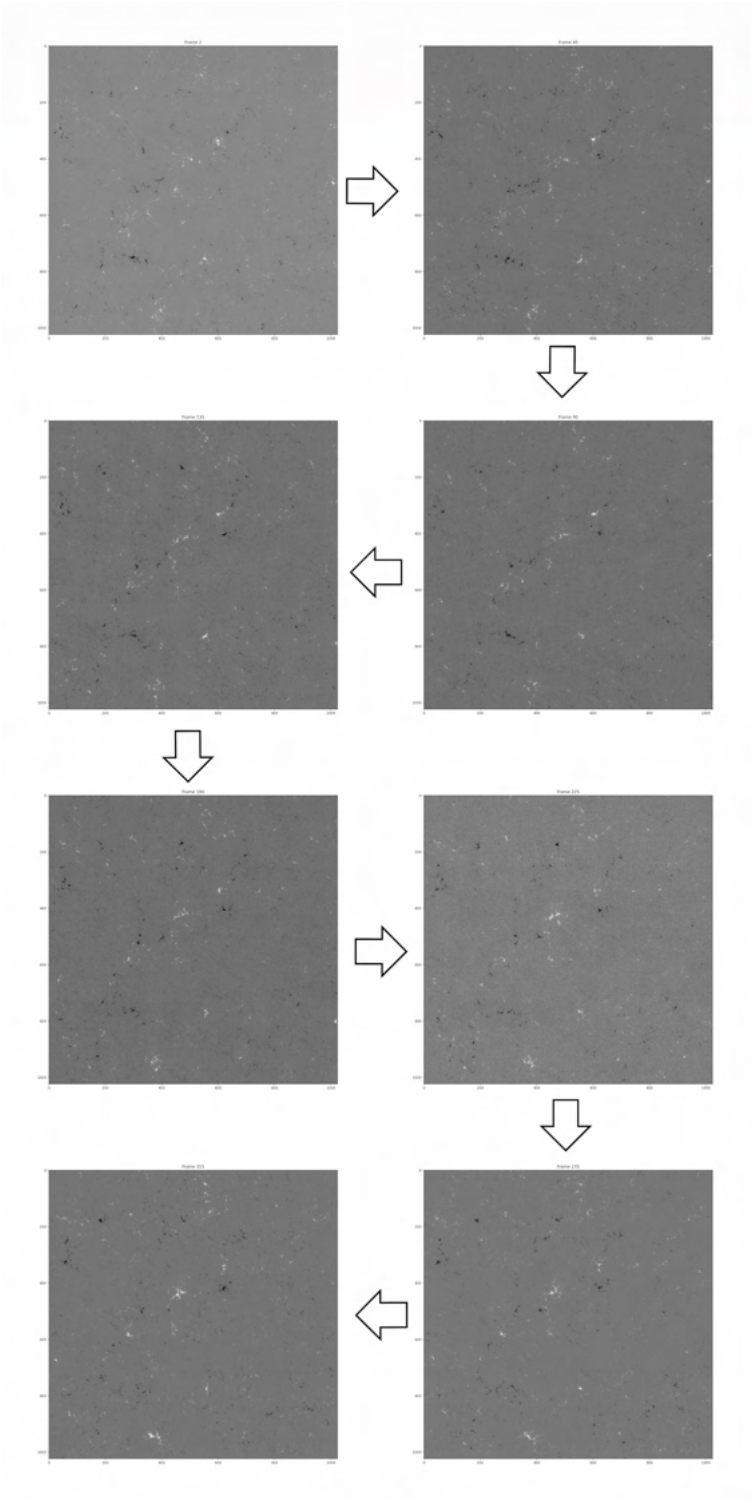

Figure 7.4: Raw data evolution of SO/PHI data

# Bibliography


[1] Anusha, L. S., et al. "Statistical evolution of quiet-Sun small-scale magnetic features using Sunrise observations." Astronomy & Astrophysics 598 (2017): A47.

[2] Solanki, S. K., Martínez Pillet, V., Vögler, A., et al. (2010). "SUNRISE: Instrument, Mission, and First Results." Astrophysical Journal Letters, 723(2), L127–L132.

[3] L. Bellot Rubio and D. Orozco Suárez, "Quiet Sun magnetic fields: an observational view," *Living Reviews in Solar Physics*, vol. 16, no. 1, pp. 1–81, 2019.

[4] Gandorfer, A., et al. (2018). "The Polarimetric and Helioseismic Imager on Solar Orbiter." Astronomy & Astrophysics, 642, A36.

[5] Zeeman, P. (1897). "On the Influence of Magnetism on the Nature of Light Emitted by a Substance." Philosophical Magazine, 43, 226-239.

[6] Kosugi, T., et al. (2007). "The Hinode (Solar-B) Mission: An Overview." Solar Physics, 243, 3-17.

[7] Rimmele, T. R., et al. (2020). "The Daniel K. Inouye Solar Telescope - Observatory Overview." Solar Physics, 295, 172.

[8] Badman, S. T. (2022). Revealing the Magnetic Structure of the Solar Corona and Inner Heliosphere in the Era of Parker Solar Probe. University of California, Berkeley.

[9] Tavabi, E., & Sadeghi, R. (2024). Exploring the Spatial Distribution and Properties of Solar Bright Points in Different Solar Areas: A Statistical Analysis of Network and Internetwork Features. Advances in Space Research.

[10] Solar Physics and Solar Wind (2021). Wiley.

[11] Orozco Suárez, D., Bellot Rubio, L. R., Martínez Pillet, V., Bonet, J. A., Vargas Domínguez, S., & del Toro Iniesta, J. C. (2010). Retrieval of solar magnetic fields from high-spatial resolution filtergraph data: the Imaging Magnetograph eXperiment (IMaX). Astronomy & Astrophysics.

[12] Bely, P. Y. (2003). The Design and Construction of Large Optical Telescopes. Springer Science and Business Media LLC.

[13] Wikipedia contributors. (n.d.). Swedish Solar Telescope. Wikipedia, The Free Encyclopedia.

[14] Rolland, J. P., Yan, C., Kim, D. W., Ma, W., Zheng, L., Zheng, L., Gu, N., Rao, C., & Qiu, Q. (2014). Design on a dual band high spectral resolution imaging solar spectrometer. International Symposium on Optoelectronic Technology and Application 2014: Imaging Spectroscopy and Telescopes and Large Optics.

[15] Ramsay, S. K., McLean, I. S., Takami, H., Elmore, D. F., Sueoka, S. R., & Casini, R. (2014). Performance of polarization modulation and calibration optics for the Daniel K. Inouye Solar Telescope. Ground-based and Airborne Instrumentation for Astronomy V.

[16] NASA. Parker Solar Probe Mission. Retrieved from . Accessed: March 24, 2025.

[17] S. Danilovic, D. Röhrbein, R. H. Cameron, and M. Schüssler, "On the relation between continuum brightness and magnetic field in solar active regions," *Astronomy & Astrophysics*, vol. 557, A52, 2013.

[18] V. Bommier, M. Martínez González, M. Bianda, H. Frisch, A. Asensio Ramos, B. Gelly, and E. Landi Degl'Innocenti, "The quiet Sun magnetic field observed with ZIMPOL on THEMIS," *Astronomy & Astrophysics*, vol. 506, no. 3, pp. 1415–1425, 2009.

[19] Solanki, S. K. (1993). Small-scale solar magnetic fields. *Space Science Reviews*, 63(1-2), 1-188.

[20] Landi Degl'Innocenti, E., & Landolfi, M. (2004). *Polarization in Spectral Lines*. Springer.

[21] Carroll, B. W., and Ostlie, D. A. (2017). *An Introduction to Modern Astrophysics* (2nd ed.). Cambridge University Press.

[22] Stix, M. (2004). *The Sun: An Introduction* (2nd ed.). Springer.

[23] Nordlund, Å., Stein, R. F., and Asplund, M. (2009). "Solar Surface Convection." *Living Reviews in Solar Physics*, **6**(1), 2.

[24] De Pontieu, B., Erdélyi, R., and James, S. P. (2004). "Solar chromospheric spicules from the leakage of photospheric oscillations and flows." *Nature*, **430**(6999), 536-539.

[25] Beckers, J. M. (1968). Solar Spicules. *Solar Physics*, **3**(3), 367–433.

[26] Rutten, R. J. (2003). *Radiative Transfer in Stellar Atmospheres*. Utrecht University Lecture Notes.

[27] Gray, D. F. (2005). *The Observation and Analysis of Stellar Photospheres* (3rd ed.). Cambridge University Press.

[28] Rees, D. E., & Semel, M. (1979). Linear polarization of the solar continuous spectrum. *Astronomy and Astrophysics*, 74, 1-5.

[29] Stenflo, J. O. (1973). Magnetic-field structure of the solar photosphere. *Solar Physics*, 32(1), 41–63.

[30] Martínez Pillet, V., Del Toro Iniesta, J. C., Álvarez-Herrero, A., Domingo, V., Bonet, J. A., González Fernández, L., et al. (2011). The Imaging Magnetograph eXperiment (IMaX) for the Sunrise Balloon-Borne Solar Observatory. *Solar Physics*, **268**, 57–102.

[31] Barthol, P., Gandorfer, A., Solanki, S. K., Schüssler, M., Chares, B., Curdt, W., ... & Knölker, M. (2011). The Sunrise mission. *Solar Physics*, 268(1), 1-34.

[32] Müller, D., St. Cyr, O. C., Zouganelis, I., Gilbert, H. R., Marsden, R., Nieves-Chinchilla, T., Antonucci, E., et al. (2020). The Solar Orbiter mission: Science overview. *Astronomy & Astrophysics*, **642**, A1.